applied optics

Compact and field-portable 3D printed shearing digital holographic microscope for automated cell identification

Siddharth Rawat,[1] Satoru Komatsu,[1] Adam Markman,[1] Arun Anand,[2] and Bahram Javidi[1,*]

[1]Electrical and Computer Engineering Department, University of Connecticut, 371 Fairfield Road Unit 2157 Storrs, Connecticut 06269, USA
[2]Applied Physics Department, Faculty of Technology and Engineering, Maharaja Sayajirao University of Baroda, Vadodara 390001, India
*Corresponding author: bahram@engr.uconn.edu

Received 12 October 2016; revised 5 February 2017; accepted 12 February 2017; posted 13 February 2017 (Doc. ID 278544); published 6 March 2017

We propose a low-cost, compact, and field-portable 3D printed holographic microscope for automated cell identification based on a common path shearing interferometer setup. Once a hologram is captured from the portable setup, a 3D reconstructed height profile of the cell is created. We extract several morphological cell features from the reconstructed 3D height profiles, including mean physical cell thickness, coefficient of variation, optical volume (OV) of the cell, projected area of the cell (PA), ratio of PA to OV, cell thickness kurtosis, cell thickness skewness, and the dry mass of the cell for identification using the random forest (RF) classifier. The 3D printed prototype can serve as a low-cost alternative for the developing world, where access to laboratory facilities for disease diagnosis are limited. Additionally, a cell phone sensor is used to capture the digital holograms. This enables the user to send the acquired holograms over the internet to a computational device located remotely for cellular identification and classification (analysis). The 3D printed system presented in this paper can be used as a low-cost, stable, and field-portable digital holographic microscope as well as an automated cell identification system. To the best of our knowledge, this is the first research paper presenting automatic cell identification using a low-cost 3D printed digital holographic microscopy setup based on common path shearing interferometry.

OCIS codes: (090.0090) Holography; (090.2880) Holographic interferometry; (170.3880) Medical and biological imaging; (170.6900) Three-dimensional microscopy; (070.5010) Pattern recognition.

https://doi.org/10.1364/AO.56.00D127

1. INTRODUCTION

Digital holographic microscopy (DHMIC) is a label-free imaging modality that enables the viewing of microscopic objects without the use of exogenous or contrast agents. DHMIC provides high axial accuracy; however, the lateral resolution is dependent on the magnification of the objective lens used. DHMIC overcomes two problems associated with conventional microscopy: the finite depth of field, which is inversely proportional to the magnification of the objective, and low contrast between the cell and the surrounding media. Cells alter the phase of the probe wavefront passing through the specimen, depending on the refractive index and thickness of the object [1–13]. Several methods have been developed to transform the phase information of the object into amplitude or intensity information [14,15], but these methods only provide qualitative information and lack quantitative information. Staining methods, such as the use of exogenous contrast agents, can enhance the image contrast, but it might change the cell morphology or be destructive. Due to the availability of fast CCD and CMOS sensors, it is possible to record digital holograms in real time [7]. The recorded holograms can be numerically reconstructed by simulating the process of diffraction using scalar diffraction, leading to the complex amplitude of the object. This complex amplitude contains the spatial phase information of the object, from which one can reconstruct the phase profile of the object. In [16], a digital holographic microscope integrated with pattern recognition algorithms was proposed for automated cell identification. A variety of digital holographic approaches have been proposed for automated cell identification [17–20].

Digital holography and microscopy are complementary techniques, and when combined, they can be useful for studying cells in a quantitative manner. To study dynamic parameters of the cell, such as cell membrane fluctuations, one needs a very stable setup because these fluctuations occur over just a few nanometers. The problem with existing digital holographic (DH) microscopy setups, which use a double path configuration,

is that the beams travel in two different arms of the interferometer and are then combined using a beam-splitter. As a result, the two beams may acquire uncorrelated phase changes due to mechanical vibrations. In comparison to two beam or double path interferometric setups, common path setups are more robust and immune to mechanical vibrations. In a common path setup, the two beams travel in the same direction, that is, the direction of beam propagation. There are many common path configurations; however, we chose the self-referencing lateral shearing configuration due to simplicity and cost-effectiveness [21–23].

In this paper, we present a low-cost, compact, and field-portable 3D printed DH imaging system that can be used for automated cell identification. The system consists of a laser source, a microscopic objective lens, a glass plate, and an imaging device (CMOS camera or a cell phone camera). The components used to build the setup are off-the-shelf optical components or printed from a 3D printer, leading to a low-cost, compact, and field-portable bio-sensing device. Once a hologram is recorded, a 3D profile reconstruction is created. Features are extracted from the reconstruction. The features are input into a pre-trained random forest classifier, which then identifies the cell. The system presented in this paper can be used as a low-cost, stable, and field-portable DH microscope and an automated cell identification system. The paper is arranged as follows. In Section 2, we give a detailed description about the common path shearing setup, the camera parameters, and the reconstruction algorithm. Experimental results are presented in Section 3, and finally, conclusions are given in Section 4.

2. MATERIAL AND METHODS

A. System Design and Camera Parameter Estimation

The schematic for the common path setup used for cell identification is shown in Fig. 1. A laser source ($\lambda = 633$ nm) illuminates the sample under inspection and a microscopic objective magnifies the sample. A fused silica glass plate splits the beam, generating two laterally sheared object beams. These two sheared beams interfere over the imaging sensor (CMOS or cell phone), and interference fringes are observed.

For the DHMIC setup in Fig. 1, the CMOS sensor used was a Thorlabs 8 bit, 5.2 μm pixel pitch, model DCC1545M, which has a large dynamic range and a 10-bit internal analog-to-digital conversion, but it transfers images to the PC with a bit depth of 8 bits to improve the readout time of the camera. For the cell phone sensor setup, a Google Nexus 5, which has an 8 MP primary camera, 1/3.2″ sensor size, and 1.4 μm pixel size, was used. Moreover, the cell phone camera uses 8 bits/channel. When comparing the camera sensor with the cell phone sensor, the dynamic range of the cell phone sensor may be lower due to the small sensor and pixel size, as the pixel wells fill quicker due to low saturation capacity. Moreover, the cell phone sensor has a Bayer filter for color detection. Finally, the cell phone camera sensor has a lower SNR than the CMOS camera. One reason is that the images generated from the cell phone camera were in the JPEG format, which is a lossy compression scheme resulting in a poorer image quality. The CMOS camera can save images as .bmp, which does not compress the images.

It is important to calculate the camera parameters. We used *ImageJ* (a public domain software: https://imagej.nih.gov/ij/) to establish an equivalence between the pixel covered by the object (also taking optical magnification into account) and the distance in microns for the cell phone sensor and CMOS. Figure 2 shows the equivalence between the pixels and the distance in microns.

The test object used in Fig. 2 is a 20-μm glass bead (SPI supplies), the other beads as observed in Fig. 2 (solid yellow boxes around the objects) are the sheared copies of the same objects. Moreover, the field of view (FOV) of the DH microscope depends on the objective and eyepiece lens used. A higher magnification objective gives a small FOV, as the sensor must image a more magnified object in comparison to a lower magnification lens; hence, a relatively smaller, magnified specimen region can be imaged on the sensor. We used 40× objective lenses with a numerical aperture (NA) of 0.65. The actual magnification depends on the placement of the camera sensor from the objective. The theoretically achievable lateral resolution with this objective is 0.595 μm. The eyepiece used with the cell phone setup has a magnification of 25×. Table 1 summarizes the parameter values for CMOS and the cell phone sensor. Figure 3 depicts the 3D printed prototype of the DH microscope.

Figure 3 is a prototype with CMOS sensor, which is analogous to the schematic shown in Fig. 1(a). To use the cell phone sensor with the 3D printed setup shown in Fig. 3, we simply replaced the CMOS with the eyepiece and the cell phone, as shown in Fig. 1(b). A cell phone adapter was 3D printed to hold the camera and eyepiece in place. This system weighs 4.62 kg with the HeNe laser and breadboard and 800 g without

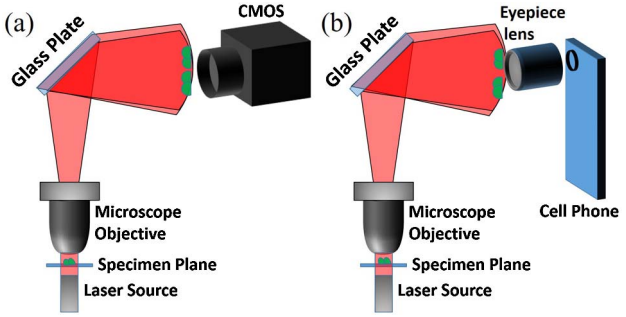

Fig. 1. Proposed single path setup (a) using a CMOS sensor and (b) using a cell phone sensor.

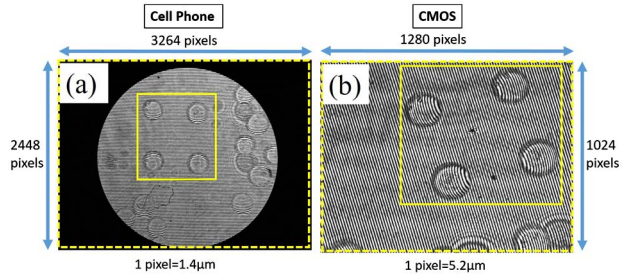

Fig. 2. FOVs of (a) a cell phone and (b) CMOS sensor used in the experiments.

Table 1. Camera Parameters

Camera Parameters	Camera Type	
	CMOS	Cell Phone Sensor
Magnification	52×	17×
Available sensor area (ASA)	35 mm^2	7.78 mm^2
Usable FOV (vertical)	104 μm	260 μm
Usable FOV (horizontal)	130 μm	260 μm
Pixel size	5.2 μm	1.4 μm
Sensor type	Mono	Color

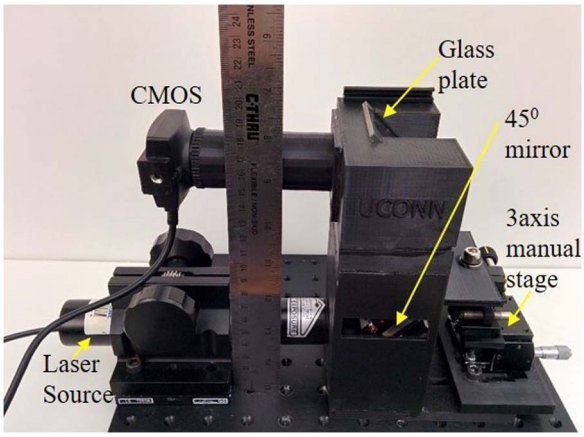

Fig. 3. 3D printed prototype of the DH microscope (with CMOS sensor) with the dimensions of 304 × 304 × 170 mm (with the breadboard). The weight of the system is 4.62 kg with the HeNe laser and breadboard and 800 g without the HeNe laser and breadboard.

the HeNe laser and breadboard. In addition, we designed and constructed a more compact 3D-printed DHMIC prototype with a smaller form factor, which is shown in Fig. 4. This system uses a laser diode (Thorlabs, CPS 635) with a wavelength of 635 nm and an elliptical beam profile in place of the HeNe laser. Moreover, the system weighs 910 g (without the base) and 1.356 kg (with the base).

In Fig. 4, the dimensions of the 3D printed DHMIC prototype are 75 × 95 × 200 mm.

B. 3D Reconstruction of Micro-Objects Using the 3D-Printed Shearing DH Setup

For the 3D printed DHMIC setup (see Fig. 3), a collimated HeNe laser beam passes through a sample that is magnified by an objective lens (40× magnification). In this DH microscope employing lateral shearing geometry, holograms, instead of shearograms, are formed at the detector [24]. This is achieved by introducing shear much larger than the magnified object image so that the images from the front and back surface of the glass plates are spatially separated. Portions of the wavefront (reflected from the front or back surface of the glass plate) unmodulated by the object information act as the reference wavefront and interfere with portions of the wavefront (reflected from the back or front surface of the glass plate) modulated by the object, which acts as the object wavefront. If the shear amount is larger than the sensor dimension, the second image (either due to reflection from the front or back surface)

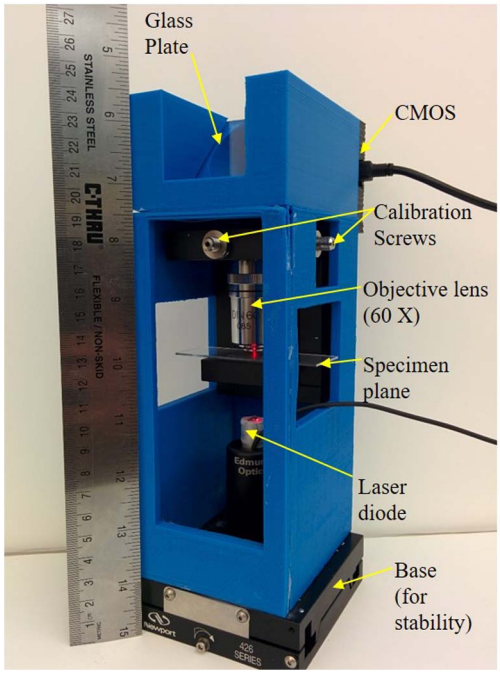

Fig. 4. Compact 3D printed prototype of the DH microscope with a laser diode with the dimensions of 75 × 95 × 200 mm. The setup weighs 910 g (without the base) and 1.365 kg (with the base).

falls outside the sensor area. If the sensor dimension is more than the shear amount, redundant information about the object is recorded. It should be noted that the full NA of the magnifying lens is utilized in the formation of the holograms. As a result, full spectral information is used in the image reconstructions, and only the NA of the imaging lens limits the imaging.

In the reconstruction, the size of the filter window of the Fourier transformed holograms needs to be limited due to unwanted sidebands. These sidebands may appear because of the non-uniform intensity variation at the detector plane, leading to a change in the contrast of the interference fringes. Another reason may be intensity image saturation leading to a non-sinusoidal fringe pattern. In addition, the size of the filter window decides the maximum spatial frequency available in the reconstructed images. In the case of CMOS sensors and cell phone cameras, the lateral resolution in the reconstructed images is not limited by the imaging lens, but by the size of the filter window. In our setup, the computed lateral resolution of the system (see Figs. 1 and 3), taking into consideration the filter window size, is approximately 1.2 μm. In addition, for the system (blue shearing setup, see Fig. 4) with the laser diode and CMOS sensor, the computed lateral resolution is 0.9 μm.

The lateral shear caused by the glass plate helps to achieve off-axis geometry, which enhances the reconstructions and simplifies the numerical processing of the digital holograms, which is not possible in in-line DHMIC setups such as Gabor holography [25]. Moreover, the carrier fringe frequency of the interferogram must not exceed the Nyquist frequency of the sensor, as the carrier fringe frequency is related to the off-axis angle caused by the lateral shear generated by the glass plate. This means the fringe frequency is a function of the thickness of the

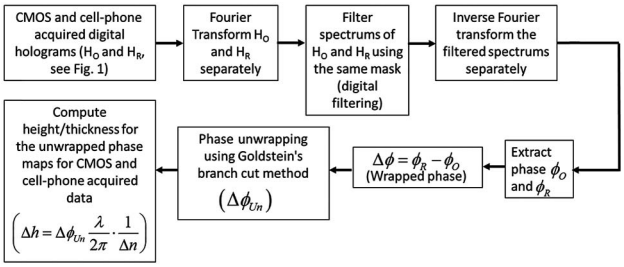

Fig. 5. Flowchart of the 3D reconstruction algorithm from the recorded hologram. $\Delta n = n_o - n_m$ is the refractive index difference between the object and surrounding medium.

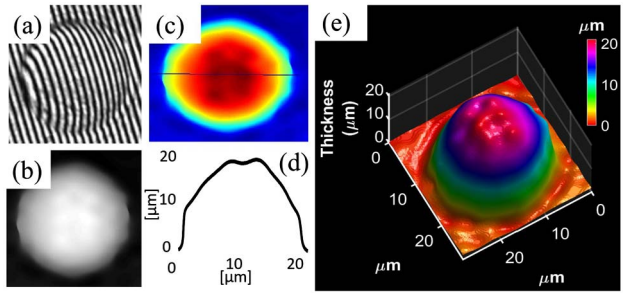

Fig. 6. Experimental results for the compact 3D printed DH microscope shown in Fig. 3 using the CMOS sensor. (a) Digital hologram of a 20-μm glass bead. (b) Unwrapped phase profile of the same bead. (c) 2D thickness profile. (d) 1D cross-sectional profile of the bead along the line shown in (c). (e) Pseudocolor 3D rendering of the thickness profile for the glass bead.

glass plate. Thus, a thicker glass plate can be used to increase the off-axis angle. The fringe frequency is $f_s = S/r\lambda$, where S denotes the lateral shift induced by the glass plate, λ is the wavelength of light source, and r is the radius of curvature of the wavefront [26]. Moreover, the relationship between shift (S), glass plate thickness (t), incidence angle on glass plate (β), and refractive index of glass (n) is given as follows: $S/t = \mathrm{Sin}(2\beta)\ (n^2 - \sin\ \beta)^{-1/2}$ [27]. Hence, a 3–5-mm glass plate is sufficient for our experiments, enabling spatial filtering the spectrum and satisfying the Nyquist criteria for sampling. To have more control over the off-axis angle, a wedge plate can be used.

The object reconstruction process is shown in Fig. 5. The Fourier transform of the digital hologram is taken, filtered (digital filtering of the real part of spectrum in Fourier domain), and then inverse Fourier transformed, generating the phase map. We recorded two holograms: one with object and background (H_O) and another with background only (H_R). We inverse Fourier transformed the filtered spectrums separately to obtain the object and background phase ($\Delta\phi_O$) and the background phase ($\Delta\phi_R$). To obtain the phase information due to object only, we subtract the phase map of object and background from the phase map with background only; this process also removes most of the system-related aberrations.

The phase was then unwrapped using the Goldstein's branch cut method [28]. After phase unwrapping, we compute the cell height/thickness [21–23,29], Δh, where $\Delta\phi_{Un}$ is the unwrapped phase difference, λ is the source wavelength, and Δn is the refractive index difference between the object and the surroundings.

3. EXPERIMENTAL RESULTS

A. Imaging Test Microspheres and Cells for the 3D Printed Setup Using a HeNe Laser

To test the performance of the system, which utilized the CMOS camera shown in Fig. 3(a), we used 20-μm glass microspheres (SPI supplies) with a mean diameter of 19.9 ± 1.4 μm and average refractive index $n_o = 1.56$. These microspheres were immersed in oil (average refractive index, $n_m = 1.518$) and then spread on a thin microscopic glass slide and covered with a thin coverslip. The digital holograms were recorded, and the 3D profiles were reconstructed using the steps mentioned in Fig. 5. In Fig. 5, $\Delta n = n_o - n_m$, is the refractive index difference between the object and surrounding medium used in the reconstruction process. The reconstruction results using the steps mentioned in Fig. 5 are implemented and shown in Fig. 6. Figure 6(a) is the digital hologram of a 20-μm glass bead, acquired using the CMOS sensor. Figure 6(b) shows the unwrapped phase profile of the bead. Figure 6(c) shows the height variations, as depicted by color maps, and Fig. 6(d) is the one-dimensional cross-sectional profile, along the line [see Fig. 6(c)]. Figure 6(e) shows the pseudocolor 3D rendering of the thickness profile for the same bead. We computed the thickness/diameter for 50 20-μm glass microspheres, where the mean diameter was 17.38 ± 1.38 μm, which was close to the thickness value specified by the manufacturer.

The experiments were repeated for biological cells, such as Diatom–Tabellaria ($n_m = 1.50$) and *E. coli* bacteria ($n_m = 1.35$). Both cell types were immersed in deionized water ($n_m = 1.33$). Figure 7(a) shows the digital hologram of the Diatom–Tabellaria cells. Figure 7(b) shows the height variations depicted by color maps, Fig. 7(c) shows the 1D cross-sectional profile of the diatom along the line, and Fig. 7(d) is the reconstructed 3D height profile for the diatom. Likewise, Figs. 7(e)–7(h) are the digital hologram, the height variations depicted by color maps, the 1D cross-sectional profile along the line [see Fig. 7(f)], and the reconstructed 3D height profile for the *E. coli* bacteria. From Fig. 7(h), one can see that the length of *E. coli* is close to 12 μm, the width is between 2–4 μm, and maximum height is 0.6 μm.

B. Imaging Test Microspheres and Cells for the More Compact 3D Printed Setup Using a Laser Diode

To show the 3D reconstruction capabilities with the more compact 3D printed DH microscope shown in Fig. 4, we implemented numerical reconstruction steps, as mentioned previously for Fig. 5. Figure 8(a) is the digital hologram of a 20-μm glass bead ($n_o = 1.56$) immersed in oil ($n_m = 1.5181$) that was acquired using the CMOS sensor. The bead diameter (obtained experimentally) is 17.427μm ± 0.9029 μm. Figure 8(b) shows the unwrapped phase profile of the bead. Figure 8(c) shows the height variations depicted by the color maps, and Fig. 8(d) is the one-dimensional cross-sectional profile along the line [see Fig. 8(c)]. Figure 8(e) shows the pseudocolor 3D rendering of the thickness profile for the same bead.

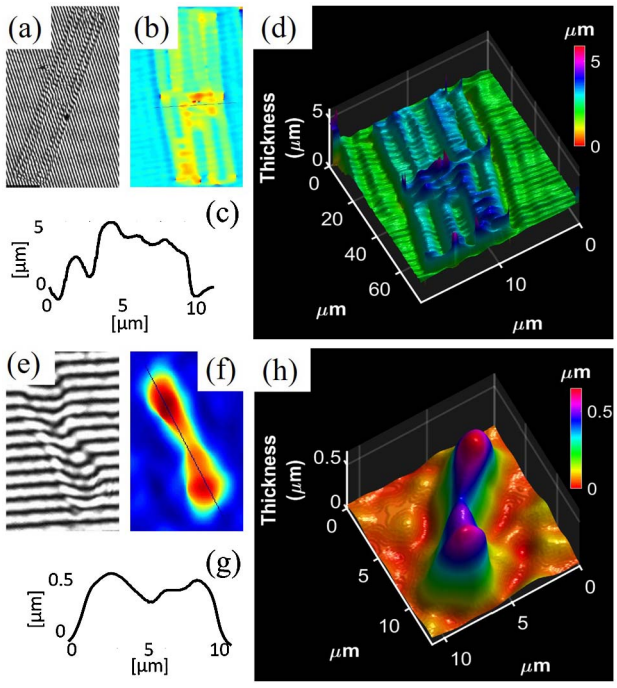

Fig. 7. (a) Digital hologram of Diatom–Tabellaria using the CMOS sensor. (b) 2D thickness profile. (c) 1D cross-sectional profile of diatom along the line shown in (b). (d) Pseudocolor 3D rendering of the thickness profile for the diatom. Likewise, (e)–(h) are the digital hologram, 2D thickness profile, 1D cross-sectional profile, and pseudocolor 3D rendering of the thickness profile for *E. coli* bacteria, respectively.

Likewise, we perform 3D reconstructions for yeast cells ($n_o = 1.53$) immersed in deionized water ($n_m = 1.33$). Figure 9(a) is the digital hologram of yeast cells immersed in distilled water acquired using the CMOS sensor. Figure 9(b) shows the unwrapped phase profile of the cells. Figure 9(c) shows the height variations depicted by color maps, and Fig. 9(d) is the one-dimensional cross-sectional profile, along the line [see Fig. 9(c)]. Figure 9(e) shows the pseudocolor 3D rendering of the thickness profile for the same cells.

In the reconstructions, roughness around and on the objects is observed. This roughness can be attributed to optical

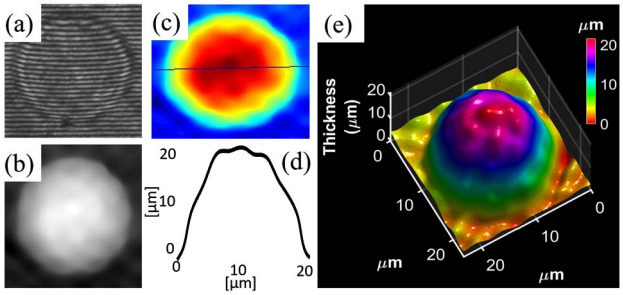

Fig. 8. Experimental results for the more compact 3D printed DH microscope as shown in Fig. 4. (a) Digital hologram of a 20-μm glass bead. (b) Unwrapped phase profile of a 20-μm glass bead and (c) 2D thickness profile. (d) 1D cross-sectional profile of the bead along the line shown in (c). (e) Pseudocolor 3D rendering of the thickness profile for the glass bead.

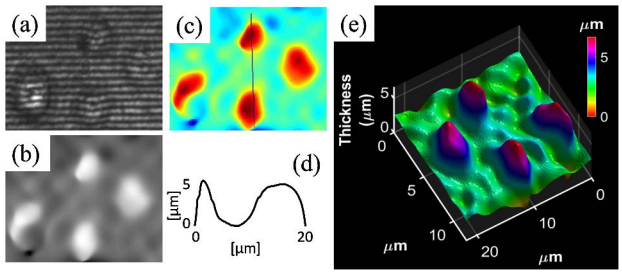

Fig. 9. Experimental results for the more compact 3D printed DH microscope shown in Fig. 4. (a) Digital hologram of yeast cells. (b) Unwrapped phase profile for the same cells. (c) 2D thickness profile. (d) 1D cross-sectional profile of the yeast cells along the line shown in (c). (e) Pseudocolor 3D rendering of the thickness profile for the yeast cells.

thickness variations. Microspheres may not be smooth. Moreover, the optical thickness variation of the object and its surroundings depends on either change in the real thickness or due to spatially changing refractive index (due to density change) in the micro-sphere and its surroundings. The size of the roughness is approximately 1–2 μm, which becomes visible as the window size becomes large enough to accommodate the spatial frequencies. One can obtain smooth reconstructions if the size of the filter window is reduced. Other possible reasons for the roughness is sample deformations and the presence of impurities.

C. Temporal Stability of the Compact 3D Printed DH Microscope Setup

Our setup (see Figs. 1 and 3) is the common path digital holography and exhibits a very high temporal stability [21] in contrast to the two beam configurations such as Michelson and Mach–Zehnder, where the two beams may acquire uncorrelated phase changes due to vibrations. To determine the temporal stability of the 3D printed prototype (Fig. 3), we recorded a series of fringe patterns or movies for a glass slide without any object. We recorded 9000 fringe patterns for 5 min at a frame rate of 30 Hz for a sensor area of 128 × 128 pixels (15.8 × 15.8 μm) using the "windowing" functionality of the CMOS sensor for the setup shown in Fig. 3. CMOS sensors can read out a certain region of interest (ROI) from the whole sensor area, which is known as windowing. One of the advantages of windowing is the elevated frame rates, which makes CMOS a favorable choice over CCDs to study the dynamic cell membrane fluctuations. One of the main reasons for using a small sensor area (128 × 128 pixels) is because processing the whole sensor area images (1280 × 1024 pixels) may be computationally expensive and time consuming. Path length changes were computed by comparing the reconstructed phase distribution for each frame (containing the fringe patterns) to a previously recorded reference background. It should be noted that the 3D-printed DHMIC prototype was not isolated against vibrations, that is, it was not placed on an air floating optical table. We computed standard deviations for a total of 16,384 (128 × 128) pixel locations. Figure 10 shows the histogram of standard deviation fluctuations with a mean standard deviation of 0.24 nm. With the 3D printed DHMIC prototype, we

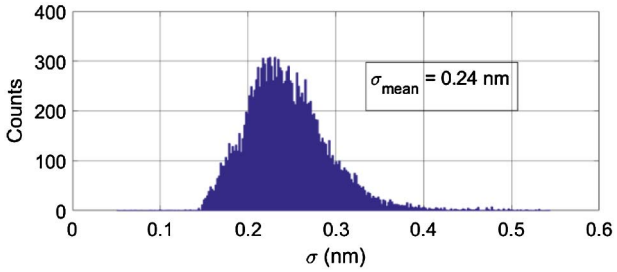

Fig. 10. Experimental results for the temporal stability of the compact 3D printed DH microscope. Histogram of standard deviations of fluctuations of 128 × 128 pixels recorded at a frame rate of 30 Hz without mechanical isolation. The inset shows the mean of standard deviations, which was 0.24 nm.

achieved sub-nanometer temporal stability of the order of 0.24 nm without any vibration isolation. This can be highly beneficial in the study involving cell membrane fluctuations, which are on the order of tens of nanometers.

D. Feature Extraction and Automated Cell Classification

From the 3D reconstructions of micro-objects, we extracted a series of features: mean physical cell thickness, coefficient of variation (COV), optical volume (OV) of the cell, projected area of cell (PA), ratio of PA to OV, cell thickness kurtosis, cell thickness skewness and the dry mass of the cell [19,30]. Before extracting these features, we applied Otsu's algorithm, which clusters based on image thresholding on the 2D unwrapped phase images. These eight features are morphological cell features that contain more information than the extracted features from the 2D bright-field microscopic images.

The random forest (RF) classifier [31] was chosen for cell identification/classification. RF is an ensemble learning method used for classification tasks. In this classifier, a decision is taken by considering the majority vote from the outputs of the decision trees consisting of nodes, branches, and leaves. Using the RF classifier, we performed classification on data obtained from the CMOS and cell phone using the setup in Figs. 1 and 3. A dataset of unwrapped phase images was created for four classes: 10-μm polystyrene bead, 20-μm glass bead, Diatom–Tabellaria fenestrate, and frog blood cell. 3D profiles were reconstructed from the CMOS acquired digital holograms by processing a total of 200 phase images (50 images per class) using the steps described in the Fig. 5. This forms the true class dataset. In addition, false class data that did not belong to any of the four classes was recorded. The false class data consisted of 3D reconstructions of digital holograms of the class of 20-μm polystyrene beads. A total of 50 false class 3D reconstructions were used. From these 3D reconstructions, we extract several cell features such as mean physical cell thickness, COV, OV of the cell, projected area of cell (PA), ratio of PA to OV, cell thickness kurtosis, cell thickness skewness, and the dry mass of the cell. After the feature extraction process, the RF classifier was trained on the true class data. The true class dataset was split in such a way that 30 reconstructions (features) from each class were used to train the classifier, and the remaining 20 were used for testing. For the RF model, 100 decision trees were used and Gini diversity index (GDI) criteria was used to form the trees from the training data. To determine the reliability of the classifier, we examined the scores or percentage of trees that voted for that class. If the scores were below 75%, we determined that the class output was not reliable, and the data was false class. Table 2 depicts the confusion matrix for the classifier, which is calculated by $(TP + TN)/N$, where TP is the number of true positives, TN is the number of true negatives, and N is the total number of test data. The classifier had an accuracy of 95.38% for CMOS-acquired data.

Table 2. Comparison of Cell Classification Results for Data Acquired Using the Setup in Fig. 1 for CMOS and Cell Phone Sensors[a]

Random Forest (RF) Classifier (CMOS Data)			Random Forest (RF) Classifier (Cell Phone Data)		
	PP	PN		PP	PN
TP	75	5	TP	75	5
TN	1	49	TN	3	47

[a]Random forest (RF) classifier was used. TP: true positive, TN: true negative, PP: predicted positive, PN: predicted negative.

We also recorded digital holograms with a cell phone sensor using the setup in Fig. 1(b) with the same micro-objects. There were 200 true and 50 false reconstructions (features). For training, 120 true reconstructions were used and 80 true and 50 false reconstructions (features) were used for testing. The classifier had an accuracy of 93.85%. Table 2 describes the confusion matrix for the cell phone sensor-based acquisition system. One reason for the marginally lower classification accuracy for the system using the cell phone sensor is that the recorded images were in the JPEG format, which is a lossy compression scheme resulting in a poorer image quality, while the CMOS camera can save images as .bmp, which does not compress the images. In addition, we note that the cell phone camera has a lower SNR than the CMOS camera. Also, the dynamic range of the CMOS is higher than the cell phone sensor due to larger sensor areas and pixel sizes. An accuracy of 93.5% using the cell phone system can be considered high enough for classification-related tasks and shows that cell phone sensors are capable of reliable hologram acquisition, which can be used for automated cell identification.

4. CONCLUSION

In summary, we designed and built a low-cost, compact, and field-portable 3D printed DH microscope (see Figs. 1, 3, and 4). The microscope requires a minimal number of off-the-shelf optical components compared to complex and sophisticated two beam setups. The 3D printed prototype exhibits a high temporal stability of the order of 0.24 nm according to our experiments, which is highly desirable in studies involving cell membrane fluctuations or to study cell dynamics. Feature extraction was performed separately for the CMOS and cell phone acquired data, and the cells were classified using the RF classifier. High accuracies for cell classification have been achieved for both CMOS and cell phone sensors. In addition, a high classification accuracy of 93.85% shows that cell phone

cameras have the potential to be used as an alternative to CMOS sensors. Thus, the 3D printed DHMIC prototype can be used with common mobile devices for hologram recording, and they produce good classification results (see Table 2). There are many advantages to using mobile devices in microscopy [32]. Using the field-portable prototype presented here, it is possible to record and send digital holograms to a computational device located remotely, via the internet for data analysis. This becomes important when the personnel handling the prototype lack the skills to process the acquired data. We believe we can further reduce the cost of the proposed device by incorporating more 3D printed components to replace mechanical components. In addition, inexpensive laser diodes and CMOS sensors, such as webcams, can be used in the setup. We envision that by making these changes, the whole setup will cost between 50–100 USD. Mass-producing the system can further reduce the cost. Our future work aims to study dynamic cell parameters, such as cell membrane vibration amplitude and vibration frequency, using the cell phone sensor for human red blood cells and diagnosis diseases using the compact setups shown in Figs. 3 and 4.

Funding. National Science Foundation (NSF) (ECCS 1545687).

Acknowledgment. We wish to acknowledge Nikon Research Corp. of America for their support of this project. B. Javidi acknowledges National Science Foundation (NSF) under grant ECCS 1545687. Adam Markman would like to acknowledge FEI and GE for their support. Satoru Komatsu would like to acknowledge Canon Inc. for their support.

REFERENCES

1. P. Memmolo, V. Bianco, F. Merola, L. Miccio, M. Paturzo, and P. Ferraro, "Breakthroughs in photonics 2013: holographic imaging," IEEE Photon. J. **6**, 701106 (2014).
2. P. Memmolo, A. Finizio, M. Paturzo, L. Miccio, and P. Ferraro, "Twin-beams digital holography for 3D tracking and quantitative phase-contrast microscopy in microfluidics," Opt. Express **19**, 25833–25842 (2011).
3. L. Miao, K. Nitta, O. Matoba, and Y. Awatsuji, "Parallel phase-shifting digital holography with adaptive function using phase-mode spatial light modulator," Appl. Opt. **51**, 2633–2637 (2012).
4. B. Javidi and E. Tajahuerce, "Three-dimensional object recognition by use of digital holography," Opt. Lett. **25**, 610–612 (2000).
5. D. Maluenda, I. Juvells, R. Martínez-Herrero, and A. Carnicer, "A digital holography technique for generating beams with arbitrary polarization and shape," Proc. SPIE **8550**, 85503Q (2012).
6. F. Dubois, L. Joannes, and J. C. Legros, "Improved three-dimensional imaging with digital holography microscope using a partial spatial coherent source," Appl. Opt. **38**, 7085–7094 (1999).
7. U. Schnars and W. Jueptner, *Digital Holography: Digital Hologram Recording, Numerical Reconstruction and Related Techniques* (Springer, 2005).
8. T. Kreis, *Handbook of Holographic Interferometry: Optical and Digital Methods* (Wiley, 2004).
9. G. Popescu, *Quantitative Phase Imaging of Cells and Tissues* (McGraw Hill, 2011).
10. P. Marquet, B. Rappaz, E. Cuche, T. Colomb, Y. Emery, C. Depeursinge, and P. Magistretti, "Digital holography microscopy: a non-invasive contrast imaging technique allowing quantitative visualization of living cells," Opt. Lett. **30**, 468–470 (2005).
11. A. Doblas, E. Sánchez-Ortiga, M. Martínez-Corral, G. Saavedra, and J. Garcia-Sucerquia, "Accurate single-shot quantitative phase imaging of biological specimens with telecentric digital holographic microscopy," J. Biomed. Opt. **19**, 046022 (2014).
12. U. Gopinathan, G. Pedrini, B. Javidi, and W. Osten, "Lensless 3D digital holographic microscopic imaging at vacuum UV wavelength," J. Display Technol. **6**, 479–483 (2010).
13. W. Osten, A. Faridian, P. Gao, K. Körner, D. Naik, G. Pedrini, A. K. Singh, M. Takeda, and M. Wilke, "Recent advances in digital holography [Invited]," Appl. Opt. **53**, G44–G63 (2014).
14. D. B. Murphy, *Fundamentals of Light Microscopy and Electronic Imaging* (Wiley, 2001).
15. F. Zernike, "Phase contrast, a new method for the microscopic observation of transparent objects," Physica **9**, 686–698 (1942).
16. B. Javidi, I. Moon, S. K. Yeom, and E. Carapezza, "Three-dimensional imaging and recognition of microorganism using single-exposure on-line (SEOL) digital holography," Opt. Express **13**, 4492–4506 (2005).
17. I. Moon and B. Javidi, "Shape tolerant three-dimensional recognition of biological microorganisms using digital holography," Opt. Express **13**, 9612–9622 (2005).
18. I. Moon, A. Anand, M. Cruz, and B. Javidi, "Identification of malaria infected red blood cells via digital shearing interferometry and statistical inference," IEEE Photonics J. **5**, 6900207 (2013).
19. A. Anand, V. K. Chhaniwal, and B. Javidi, "Imaging embryonic stem cell dynamics using quantitative 3-D digital holographic microscopy," IEEE Photonics J. **3**, 546–554 (2011).
20. D. Shin, M. Daneshpanah, A. Anand, and B. Javidi, "Optofluidic system for three-dimensional sensing and identification of microorganisms with digital holographic microscopy," Opt. Lett. **35**, 4066–4068 (2010).
21. A. S. Singh, A. Anand, R. A. Leitgeb, and B. Javidi, "Lateral shearing digital holographic imaging of small biological specimens," Opt. Express **20**, 23617–23622 (2012).
22. V. K. Chhaniwal, A. S. G. Singh, R. A. Leitgeb, B. Javidi, and A. Anand, "Quantitative phase-contrast imaging with compact digital holographic microscope employing Lloyd's mirror," Opt. Lett. **37**, 5127–5129 (2012).
23. A. Anand, A. Faridian, V. K. Hhaniwal, S. Mahajan, V. Trivedi, S. K. Dubey, G. Pedrini, W. Osten, and B. Javidi, "Single beam Fourier transform digital holographic quantitative phase microscopy," Appl. Phys. Lett. **104**, 103705 (2014).
24. K. B. Seo, B. M. Kim, and E. S. Kim, "Digital holographic microscopy based on a modified lateral shearing interferometer for three-dimensional visual inspection of nanoscale defects on transparent objects," Nanoscale Res. Lett. **9**, 471 (2014).
25. J. Garcia-Sucerquia, W. Xu, S. K. Jericho, P. Klages, M. H. Jericho, and H. J. Kreuzer, "Digital in-line holographic microscopy," Appl. Opt. **45**, 836–850 (2006).
26. R. P. Shukla and D. Malacara, "Some applications of the Murty interferometer: a review," Opt. Lasers Eng. **26**, 1–42 (1997).
27. D. Malacara, "Testing of optical surfaces," Ph.D. dissertation, Institute of Optics (University of Rochester, 1965).
28. R. M. Goldstein, H. A. Zebker, and C. L. Werner, "Satellite radar interferometry: two-dimensional phase unwrapping," Radio Sci. **23**, 713–720 (1988).
29. A. Anand, V. K. Chhaniwal, N. R. Patel, and B. Javidi, "Automatic identification of malaria-infected RBC with digital holographic microscopy using correlation algorithms," IEEE Photon. J. **4**, 1456–1464 (2012).
30. Y. Kim, H. Shim, K. Kim, H. Park, S. Jang, and Y. Park, "Profiling individual human red blood cells using common-path diffraction optical tomography," Sci. Rep. **4**, 6659 (2014).
31. L. Breiman, "Random forests," Mach. Learn. **45**, 5–32 (2001).
32. J. C. Contreras-Naranjo, Q. Wei, and A. Ozcan, "Mobile phone based microscopy, sensing, and diagnostics," IEEE J. Sel. Top. Quantum Electron. **22**, 392–405 (2016).